Dynamic response of $Cu_{46}Zr_{54}$ metallic glass to high-strain-rate shock loading: Plasticity, spall, and atomic-level structures

Bedri Arman,[1,2] Sheng-Nian Luo,[1,*] Timothy C. Germann,[1] and Tahir Çağın[2,†]
[1]*Los Alamos National Laboratory, Los Alamos, New Mexico 87545, USA*
[2]*Department of Chemical Engineering, Texas A&M University, College Station, Texas 77845, USA*
(Received 3 November 2009; revised manuscript received 11 January 2010; published 15 April 2010)

We investigate dynamic response of $Cu_{46}Zr_{54}$ metallic glass under adiabatic planar shock wave loading (one-dimensional strain) with molecular dynamics simulations, including Hugoniot (shock) states, shock-induced plasticity, and spallation. The Hugoniot states are obtained up to 60 GPa along with the von Mises shear flow strengths, and the dynamic spall strengths, at different strain rates and temperatures. The spall strengths likely represent the limiting values achievable in experiments such as laser ablation. For the steady shock states, a clear elastic-plastic transition is identified (e.g., in the shock velocity-particle velocity curve), and the shear strength shows strain softening. However, the elastic-plastic transition across the shock front displays transient stress overshoot (hardening) above the Hugoniot elastic limit followed by a relatively sluggish relaxation to the steady shock state, and the plastic shock front steepens with increasing shock strength. The local von Mises shear strain analysis is used to characterize local deformation, and the Voronoi tessellation analysis, the corresponding local structures at various stages of shock, release, tension and spallation. The plasticity in this glass, manifested as localized shear transformation zones, is of local structure rather than thermal origin, and void nucleation occurs preferentially at the highly shear-deformed regions. The Voronoi and shear strain analyses show that the atoms with different local structures are of different shear resistances that lead to shear localization (e.g., the atoms indexed with $\langle 0,0,12,0\rangle$ are most shear-resistant, and those with $\langle 0,2,8,1\rangle$ are highly prone to shear flow). The dynamic changes in local structures are consistent with the observed deformation dynamics.

DOI: 10.1103/PhysRevB.81.144201 PACS number(s): 62.50.Ef

I. INTRODUCTION

Metallic glasses are of great interest for their superior mechanical and chemical properties as well as deformation mechanisms, and a subject of tremendous experimental, theoretical and modeling efforts.[1–5] Such materials behaviors as plastic deformation are normally loading-dependent; low strain rate experiments and high strain rate molecular dynamics (MD) simulations often adopt one-dimensional (1D) stress (tension or compression), pure shear and instrumented indentation under isothermal conditions,[4–16] to characterize mechanical and physical properties of various metallic glasses and understand the underlying physics, including shear localization and banding, and strain softening and hardening.[3–5]

Complementary to 1D stress, pure shear, indentation, ion radiation loading,[17] and the alike, planar shock wave loading[18–22] induces adiabatically 1D strain and is a most useful technique to investigate dynamic materials response at high strain rates. Of particular interest are shock-induced plasticity and spall damage.[20,21,23] Dynamic properties of several metallic glasses were explored with gas-gun type shock wave experiments.[24–28] On the other hand, MD can simulate shock wave loading[29,30] for studying equation of state, plasticity or spall damage, and serve as a complement to and may overlap in strain rates with shock wave experiments such as laser ablation.[31,32] MD simulations are also advantageous in revealing atomic-scale structure evolution and related physics.[33–36] Previous MD shock simulations were largely performed on single crystal and nanocrystalline elemental metals, alloys, and ceramic glasses.[35–44] However, such simulations are underexplored overall, and the shock response of metallic glasses has barely been addressed with MD. In this study, we choose a simple binary alloy, $Cu_{46}Zr_{54}$, as a model system and perform MD shock simulations to shed light on the shock response of bulk metallic glasses. This glass was developed recently and modeled with MD simulations.[45,46] The shock response includes the Hugoniot (shock) states, shock-induced plasticity and spallation. We characterize the shear deformation and short-range structure features with von Mises shear strain[11] and Voronoi tessellation analysis,[47,48] as well as shear flow strength and spall strength. We find that the plastic flow is initiated with heterogeneous localized shear deformation that can be attributed to short-range structure features characteristic of such metallic glasses, and void nucleation occurs preferentially at highly shear-deformed regions.

Section II of this presentation addresses the methodology related to MD simulations and the deformation and structure analysis methods (the local von Mises shear strain, von Mises shear flow strength and Voronoi tessellation). The results and discussion are presented in Sec. III including the Hugoniot states, plasticity, spall, the mechanisms for plasticity and spallation as well as the related structural features, followed by conclusions in Sec. IV.

II. METHODOLOGY

To describe the Cu-Cu, Zr-Zr, and Cu-Zr interactions in the Cu-Zr alloys, we adopt the Finnis-Sinclair type interatomic potential[49] developed by Mendelev *et al.*[50] For a sys-

tem with N atoms, the total potential energy U consists of a pairwise term and a many-body term

$$U = \sum_{i=1}^{N-1} \sum_{j=i+1}^{N} \varphi_{t_i t_j}(r_{ij}) + \sum_{i=1}^{N} \Phi_{t_i}(\rho_i). \quad (1)$$

Here, t_i (t_j) is the element type of atom i (j), φ is the pairwise potential between atoms i and j separated by a distance r_{ij}, Φ is the embedded energy functional, and the electronic density is

$$\rho_i = \sum_j \psi_{t_i t_j}(r_{ij}). \quad (2)$$

Analytical expressions have been obtained for φ, Φ and ψ (eight functions in total) via fitting to some known properties of pure elements and *ab initio* Cu-Zr formation energies.[50] This potential reproduces experimental x-ray diffraction data on amorphous Cu-Zr alloys, and predicts reasonably well the elastic moduli.[50,51]

Our MD simulations are performed with the LAMMPS package.[52] The initial configuration, composed of 4000 atoms with randomized positions, is subjected to incremental heating to 2000 K and then cooling to 300 K at ambient pressure, and forms a $Cu_{46}Zr_{54}$ metallic glass. The constant-pressure-temperature (NPT) ensemble and three-dimensional periodic boundary conditions are applied. The time step for integrating the equation of motion is 2 fs. The heating and cooling rates are 20–100 K per 20–100 ps, i.e., 0.2–5 K ps^{-1}. This glass is further equilibrated for 100 ps at ambient conditions, and achieves an atomic volume of 18.47 Å^3, corresponding to an initial (ambient) density of ρ_0=7.06 g cm^{-3}. We calculate the radial distribution functions (RDF) of this glass. Both RDFs and ρ_0 are consistent with previous results predicted from the same potential.[50,51] Mendelev *et al.*[51] also computed the elastic constants of CuZr glasses at ambient conditions, and the bulk modulus $B \approx 116$ GPa and shear modulus $\mu \approx 21$ GPa for $Cu_{46}Zr_{54}$. Thus, the Poisson's ratio $\nu \approx 0.415$; the bulk and longitudinal sound velocities are c_B=4.0 km s^{-1} and c_L=4.5 km s^{-1}, respectively. This 4 000-atom glass is replicated along three orthogonal directions and equilibrated further with the NPT ensemble at ambient conditions for shock simulations on larger systems, in order to remove possible artifacts from the replication process. The structures of the resulting glasses are indistinguishable from that of the small system. The exact glass structure may vary modestly overall for small changes in cooling rate and relaxation process affordable by current MD simulations,[13] and Duan *et al.* showed recently that the cooling rates (similar to ours) have a slight effect on such properties as the glass transition temperature.[45] We expect that our simulations with current glass configuration largely represent general features of the dynamic response of metallic glasses to shock loading.

Planar shock-spall simulations are conducted with the flyer plate-target configuration described below and the microcanonical ensemble.[29,36] The shock loading is along the x axis. Periodic boundary conditions are applied only along the y and z axes, and thus free surfaces normal to the x axis are present on the nonimpact sides of the flyer and target. The flyer and target are constrained along the y and z axes, but can undergo compression or tension along the x axis. Such loading induces 1D strain as in planar shock wave experiments.[18–22] The time step for integrating the equation of motion is 1 fs, and the run durations are 50–200 ps.

In most of our simulations, the target consists of 768 000 atoms (approximately 8.4 nm × 8.4 nm × 200 nm in edge lengths). The flyer plate has the same cross-section area as the target, and its length is reduced by half (384 000 atoms). In addition, cross-section areas of 4.2 nm × 4.2 nm and 16.8 nm × 16.8 nm are explored to examine the (cross-sectional) size effect on plasticity and the results are similar; a target length of 1.2 μm is also attempted for better separating the elastic precursor and the plastic shock. We denote the desired steady shock state particle velocity as u_p. The flyer plate and target are assigned initial velocities of $\frac{4}{3}u_p$ and $-\frac{2}{3}u_p$, respectively, before impacting each other, so that the flyer-target system has zero center-of-mass velocity. The impact yields shock waves propagating into the target and the flyer plate, which are then reflected at the respective free surfaces as centered simple rarefaction (release) fans, and their interaction induces an evolving tensile region and spall in the target (for sufficiently strong shocks). The free surface velocity vs time (t) is obtained from the particle velocity evolution on the target free surface as $u_{fs}(t)$. The atomic stress tensor σ_{ij} is calculated from the atomic virial and thermal velocity (i, j=1, 2, and 3, corresponding to x, y, and z, respectively). The binning analysis[36] is used to obtain mass density (ρ), stress (σ_{ij}), particle velocity (u), and temperature (T) profiles along the x axis.

Two techniques for characterizing the short-range order in amorphous metallic glasses are the Honeycutt-Andersen analysis[45,53] and the Voronoi tessellation analysis,[47,48,54,55] and the latter is adopted here. In the Voronoi analysis, each atom is indexed with the Voronoi indices, $i,j,k,l,\ldots$, characteristic of the Voronoi polyhedron centered at this atom and consisting of its nearest neighbors (as determined from the first minimum in RDF). The center atoms can be Cu or Zr. Four indices are sufficient for our purpose, and the integers i, j, k, and l denote the numbers of Voronoi polygons, namely, triangle, tetragon, pentagon, and hexagon obtained via the Voronoi polyhedron decomposition, respectively; their sum corresponds to the coordination number (CN) of the center atom. For the $Cu_{46}Zr_{54}$ metallic glass, a total of seven types of Voronoi indices are considered: $\langle 0,0,12,0\rangle$, $\langle 0,2,8,2\rangle$, $\langle 0,2,8,1\rangle$, $\langle 0,3,6,3\rangle$, $\langle 0,3,6,4\rangle$ and $\langle 0,1,10,2\rangle$, referred to as Types 1–6, respectively; other minor individual types are denoted collectively as Type 7. Types 1 (CN=12, full icosahedron) and 6 (CN=13) represent the densest packing and Type 1 has highest shear resistance.[54] Types 2 and 4 are considered as distorted icosahedral structures with CN=12. Type 3 is similar to Type 2 but with CN=11. Types 5 and 6 have the highest CN (13) among Types 1–6.

As demonstrated by Shimizu *et al.*,[11] a useful parameter to characterize the shear flow in metallic glasses is the von Mises type shear strain, η^{vM}, defined for each atom i between the present and a reference configuration. The number of the nearest neighbors of atom i in the reference configuration (denoted with superscript 0; it is the unshocked con-

TABLE I. Shock and spall parameters for the $Cu_{46}Zr_{54}$ glass. The target dimensions are $8.4\times8.4\times200$ nm^3. The units for velocity, stress, temperature, and strain rate are km s^{-1}, GPa, K, and 10^9 s^{-1}, respectively.

u_p	$\sigma_{11,H}$	$\sigma_{22,H}$	$\sigma_{33,H}$	σ_Y	ν	h	T_H	T_{sp}	σ_{sp}	$\dot{\varepsilon}$
0.125	4.22	3.06	3.04	…	0.420	0.82	315	300	4.0[a]	…
0.250	8.39	6.32	6.34	1.98	0.432	0.84	330	305	6.8[a]	…
0.375	12.32	10.29	10.33	2.01	0.456	0.89	350	330	9.0[a]	…
0.500	16.33	14.62	14.56	1.74	0.472	0.93	380	370	10.6	1.8
0.750	25.22	24.17	24.14	1.06	0.489	0.97	480	450	11.0	8.6
1.000	35.57	35.00	35.02	0.56	0.496	0.99	600	550	11.2	17.4
1.500	59.75	59.64	59.66	0.10	0.499	1.00	1200	870	9.6	26.2

[a]The maximum tensile stress achieved; no spallation.

figuration unless stated otherwise) is n_i^0, and the vector separation between atom i and each of its neighbors j is $\mathbf{d}_{ij}$. We seek a locally affine transformation matrix $\mathbf{J}_i$ which maps

$$\{\mathbf{d}_{ji}^0\} \rightarrow \{\mathbf{d}_{ji}\}, \quad \forall\, j \in n_i^0, \tag{3}$$

and minimizes

$$\sum_{j\in n_i^0} |\mathbf{d}_{ji}^0\mathbf{J}_i - \mathbf{d}_{ji}|^2. \tag{4}$$

The strain matrix follows as

$$\boldsymbol{\eta}_i = \frac{1}{2}(\mathbf{J}_i\mathbf{J}_i^{\mathrm{T}} - \mathbf{I}), \tag{5}$$

where $\mathbf{I}$ is the unit matrix, and the local shear strain for atom i (a scalar) is

$$\eta_i^{\mathrm{vM}} = \left\{\frac{1}{6}[(\eta_{11}-\eta_{22})^2 + (\eta_{22}-\eta_{33})^2 + (\eta_{33}-\eta_{11})^2] + \eta_{12}^2 + \eta_{23}^2 + \eta_{31}^2\right\}^{1/2}. \tag{6}$$

We use the von Mises yield criterion[56] to define the yield strength under shock compression

$$\sigma_Y \equiv \sqrt{3J_2}, \tag{7}$$

where the second deviatoric stress invariant

$$J_2 = \frac{1}{6}[(\sigma_{11}-\sigma_{22})^2 + (\sigma_{22}-\sigma_{33})^2 + (\sigma_{33}-\sigma_{11})^2] + \sigma_{12}^2 + \sigma_{23}^2 + \sigma_{31}^2. \tag{8}$$

σ_Y is equivalently the yield stress under uniaxial stress.

The effective Poisson's ratio at a shock state is related to the effective Lamé's constants (λ and μ) as

$$\nu = \frac{\lambda}{2(\lambda+\mu)}. \tag{9}$$

For isotropic metallic glasses under 1D strain loading, we have essentially $\sigma_{11} \geq \sigma_{22} = \sigma_{33}$ (principal stresses), $\sigma_{12} = \sigma_{23} = \sigma_{31} = 0$, and

$$\sigma_{11} = (\lambda + 2\mu)\varepsilon, \tag{10}$$

and

$$\sigma_{22} = \sigma_{33} = \lambda\varepsilon, \tag{11}$$

where ε denotes the bulk strain. It follows from Eqs. (9)–(11) that

$$\nu = \frac{\sigma_{22}}{\sigma_{11}+\sigma_{22}}, \tag{12}$$

and σ_{22} is taken as the average of σ_{22} and σ_{33} directly measured in MD simulations. We also define hydrostaticity (h) for a given shock state as

$$h \equiv \frac{\sigma_{11}+\sigma_{22}+\sigma_{33}}{3\sigma_{11}}. \tag{13}$$

III. RESULTS AND DISCUSSION

A. Hugoniot states, plasticity, and spallation phenomena

MD shock simulations are explored for $0.125 \leq u_p \leq 1.5$ km s^{-1}, yielding results on elastic and plastic deformation, shear strengths, supported shock states (Hugoniot states) and spallation (Table I and Figs. 1–7).

The wave propagation and interactions related to shock, release, tension and spall are illustrated with density evolution as viewed in a traditional $x-t$ diagram (Fig. 1). The

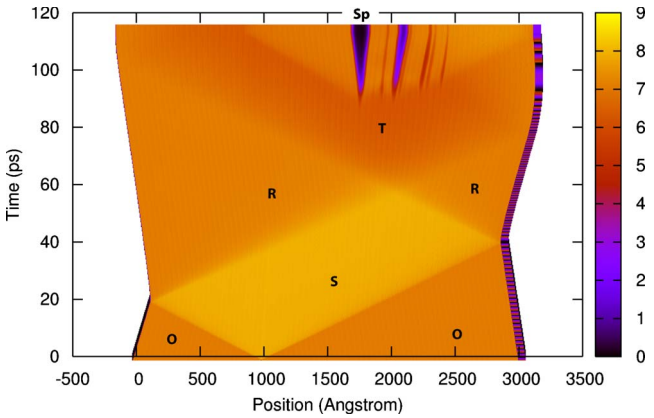

FIG. 1. (Color online) The $x-t$ diagram for shock loading of the $Cu_{46}Zr_{54}$ glass with $u_p=0.5$ km s^{-1}. Color coding is based on local mass density $\rho(x)$ in g cm^{-3}. Region *O*: unshocked; *S*: shocked; *R*: release; *T*: tension; *Sp*: spall.

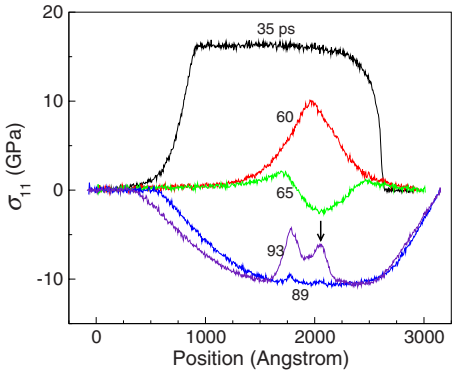

FIG. 2. (Color online) The stress profiles for $u_p=0.5$ km s^{-1} at selected instants showing sequentially shock, release, tension and spallation. The arrow denotes an example of spallation.

impact-induced shocks, the subsequent release waves originating at free surfaces and the interaction of the opposing release waves, yield well-defined shock, release, tensile and spall regimes in the $x-t$ diagram. Figure 2 shows the corresponding stress profiles at selected t with a spall zone indicated. Upon spall, the tensile stress is reduced, inducing (re-)compression waves propagating toward the free surfaces. This shock-release-spall sequence is also manifested in the free surface velocity history (Fig. 3) similar to experimental measurements with the velocity interferometry.[57] In particular, the recompression following spall is registered in $u_{fs}(t)$ as a pullback characteristic of spallation.

A shocked solid undergoes plastic deformation at or above the Hugoniot elastic limit (HEL), and a two-wave structure (the elastic precursor and the plastic shock wave) is expected until the elastic precursor is overtaken by the plastic shock at high shock strengths. Below HEL, there exists only a single elastic shock. A two-wave structure can be identified in $u_{fs}(t)$ and $\sigma_{11}(x)$ for $u_p=0.5$ km s^{-1}; the sluggish plastic wave front following the rapidly rising elastic precursor is characteristic likely due to its particular plastic deformation mechanism different from conventional crystal plasticity[58] [Figs. 3 and 4(a)]. At higher shock strengths (e.g., $u_p=1$ km s^{-1}, Fig. 3), the plastic shock overtakes the elastic precursor (the two-wave structure then becomes one-wave)

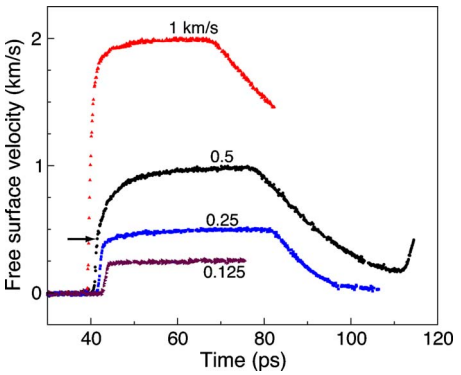

FIG. 3. (Color online) Representative free surface velocity histories for different u_p (numbers). The arrow indicates the elastic precursor. Spall pullback in u_{fs} occurs at $t\sim112$ ps for $u_p=0.5$ km s^{-1}.

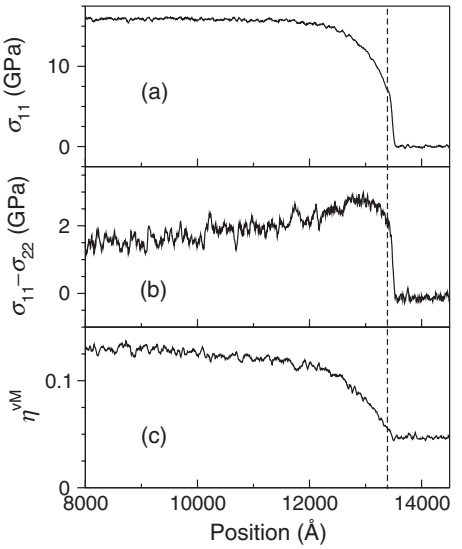

FIG. 4. σ_{11}, $(\sigma_{11}-\sigma_{22})$ and η^{vM} profiles across the shock front in the target for $u_p=0.5$ km s^{-1} at $t=169$ ps. The dashed line indicates the onset of the elastic-plastic transition at HEL. There exists a stress overshoot in (b) after HEL. The target dimensions are 4.2 nm$\times$4.2 nm$\times$1.2 μm.

and the plastic shock rise is much faster because of the facilitated kinetics of the elastic-plastic transition. The rounded transition from the shock rise to the plateau is observed near and above HEL for this metallic glass (e.g., $u_p=0.25$ km s^{-1}, Fig. 3), and below HEL, the rounding is less pronounced but the shock rise is shallower ($u_p=0.125$ km s^{-1}). Similarly, such rounding above HEL was reported for some Zr-based metallic glasses.[25,28] Interestingly, Kanel *et al.* observed this rounding even below HEL for some shocked silicate glasses.[59,60] However, there are some exceptions.[24] We speculate that free volume and shear deformation kinetics may play a role in this rounding behavior (below and above HEL), although the exact mechanisms remain to be explored. The plateau feature in our simulations is different from the experiments on Zr-based metallic glasses,[24,25,28] possibly because of the differences in time scale.

The wave speed of the leading wave front at a given u_p, u_{s1}, can be obtained from two wave profiles at different t and

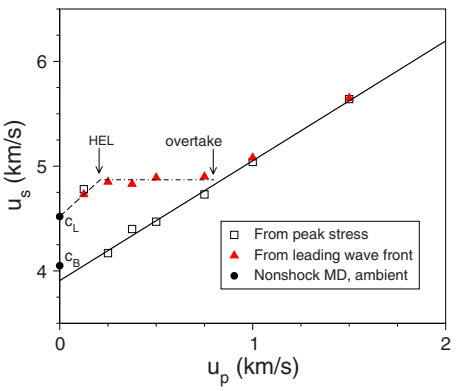

FIG. 5. (Color online) The shock velocity (u_s, squares) along with the leading wave front velocity (triangles) plotted as a function of u_p. c_L and c_B are deduced from Ref. 51.

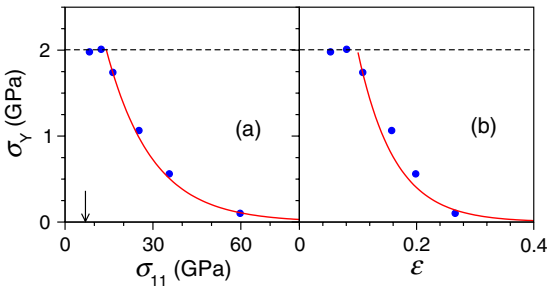

FIG. 6. (Color online) The shock-state yield strength σ_Y as a function of peak stress (a) and volumetric strain (b). Solid curves: power-law fits showing strain softening. Dashed line: the elastic-perfectly plastic transition. Arrow: HEL.

is plotted in Fig. 5 (triangles); it thus represents the elastic and plastic shock speeds before and after the overtake of the elastic precursor by the plastic shock, respectively. Three regimes can be identified (divided by HEL and the overtake): below HEL (regime I), u_{s1} increases with increasing u_p from the ambient longitudinal wave speed; between HEL and the overtake (regime II), u_{s1} remains a constant (4.87 ± 0.03 km s^{-1}) since the elastic-plastic transition occurs at the same stress level; above the overtake (regime III), u_{s1} increases again with u_p. The HEL is located between 0.125 and 0.25 km s^{-1}, and the overtake occurs at $u_p \approx 0.8$ km s^{-1}. The HEL can be measured more accurately as the amplitude of the particle velocity or σ_{11} of the elastic precursor [e.g., from $\sigma_{11}(x)$ and $u_{fs}(t)$]: σ_{HEL} is about 7.2 ± 0.4 GPa [Fig. 4(a)] and $u_{p,HEL}$ is about 0.21 ± 0.01 km s^{-1} (Fig. 3; the particle velocity doubles on the free surface); they are consistent with each other using the momentum conservation jump condition[22]

$$\sigma_{HEL} = \rho_0 u_s u_p|_{HEL}, \tag{14}$$

and $u_s = 4.87$ km s^{-1}. The HELs of some Zr-based metallic glasses determined from shock experiments are between 5–7 GPa (mostly around 7 GPa),[25–28] consistent with our simulations here. Linear extrapolation of the values of u_{s1} at and below HEL to $u_p = 0$ yields 4.5 km s^{-1}; this value is essentially the longitudinal sound speed (c_L) at ambient condition, and agrees with the previous result.[51]

The shock plateau is largely developed as seen from the free surface velocity histories or the wave profiles within the bulk, from which the supported shock or Hugoniot states (H) at a given u_p can be deduced, including σ_{ij}, ρ, and T as well as shock velocity u_s (Table I and Fig. 5). In regimes I and III (with a single elastic and plastic shock wave, respectively), the Hugoniot jump condition is applied between the ambient and final shock states

$$\sigma_{11,H} = \rho_0 u_s u_p. \tag{15}$$

In regime II with split elastic and plastic waves, we consider two successive applications of the jump condition: from the ambient condition to the HEL [Eq. (14)], and from the HEL to the final plastic shock state,

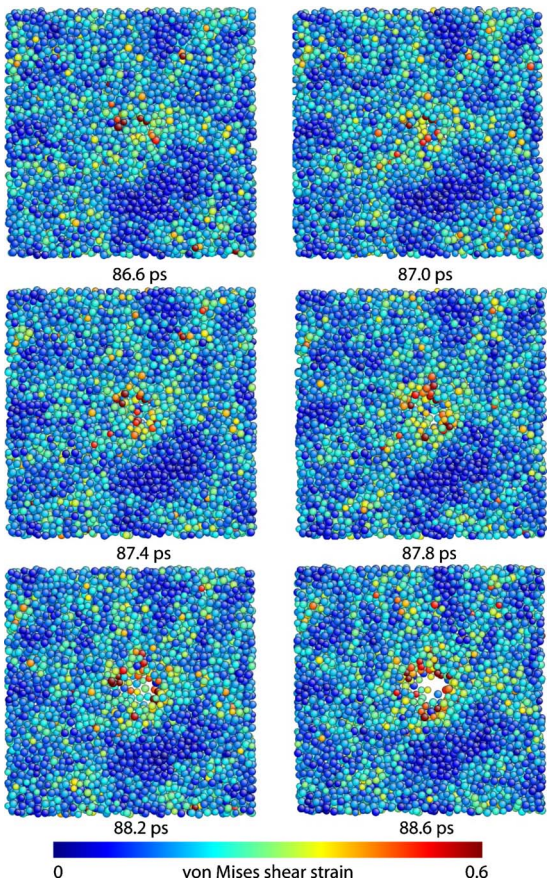

FIG. 7. (Color online) Snapshots of the atomic configurations (8.4 nm × 8.4 nm cross-section) showing early stages of void nucleation and growth for $u_p = 0.5$ km s^{-1}, viewed along the shock direction. Visualization adopts AtomEye.[62]

$$\sigma_{11,H} - \sigma_{11,HEL} = \rho_{HEL}(u_s - u_{p,HEL})(u_p - u_{p,HEL}). \tag{16}$$

In contrast to u_{s1}, direct measurement of u_s is difficult due to the sluggish elastic-plastic transition (as well as computational limitations on the simulation size). u_s is calculated with Eqs. (15) and (16) instead. u_s becomes u_{s1} in the elastic and overtake regimes as expected (Fig. 5). Note that Eq. (16) is intended for steady flows and only approximate in our cases. The peak shock state u_s–u_p relation for the plastic wave can be described with a linear fitting

$$u_s = c_0 + s u_p, \tag{17}$$

where $c_0 = 3.91 \pm 0.04$ km s^{-1} and $s = 1.14 \pm 0.03$ (the solid line, Fig. 5). Fitting to all the data points in the plastic region or those at $u_p \geq 0.75$ km s^{-1} yields the same results. c_0 is the extrapolated u_s at $u_p = 0$, and is in reasonable agreement with a previous result of the bulk sound speed c_B (4.0 km s^{-1}) at the ambient condition[51] within simulation uncertainties. The volumetric strain

$$\varepsilon \equiv 1 - \frac{\rho_0}{\rho_H}, \tag{18}$$

where ρ_H is obtained with the mass conservation jump condition[22] from u_s and u_p. Direct measurement of ρ_H from $\rho(x)$ yields consistent results.

A shocked solid begins to yield when σ_{11} reaches the critical value σ_{HEL}, above which it may retain a constant shear strength (the elastic-perfectly plastic transition), or σ_Y may decrease (strain softening), or increase (strain hardening) with increasing shock strength. We examine the differential stress, or $2\tau=(\sigma_{11}-\sigma_{22})$, across the shock front and σ_Y at the supported shock states. τ is the maximum shear stress, and $\sigma_Y=2\tau$ for plastic deformation.

Across the shock front, the solid is elastically shocked to σ_{HEL}; the elastic shock is succeeded by a sluggish transition to plastic shock state [e.g., $u_p=0.5$ km s^{-1}, Fig. 4(a)]; correspondingly, $2\tau=(\sigma_{11}-\sigma_{22})$ rises sharply in the elastic regime to about 2 GPa, overshoots to about 2.7 GPa (strain hardening) and then relaxes slowly to a steady value of about 1.7 GPa at the steady shock state. Note that this strain hardening is highly transient compared to the ensuing relaxation, i.e., the latter is a dominant feature of the plasticity kinetics.

Assuming the von Mises yield criterion, σ_Y is also estimated at the supported shocked states above HEL (Table I and Fig. 6) as a function of $\sigma_{11,H}$ or ε_H, and shows a power-law softening in both cases. The softening is emerging only at $u_p=0.5$ km s^{-1}, i.e., with a delay relative to HEL, and becomes drastic around 0.75 km s^{-1}. Since shock loading is adiabatic with an accompanying temperature rise, thermal softening is coupled with strain softening at higher shock strengths (e.g., at u_p above 1 km s^{-1}). This strain softening in metallic glasses has also been observed in quasistatic loading conditions such as nanoindentation,[4,5,61] and is likely due to the formation of shear transformation zones (see below) and the lack of efficient strain hardening mechanisms.[5] σ_Y approaches zero at high shock strengths (e.g., $u_p=1.5$ km s^{-1}), and the plastic wave overtakes the elastic wave at $u_p>0.75$ km s^{-1}. Such features are unlikely caused by melting since T_H is too low at these elevated stresses (Table I), but more likely due to the high Poisson's ratio and the applied stresses.

At the HEL, it follows from the von Mises yield criterion that

$$\sigma_Y=\frac{1-2\nu}{1-\nu}\sigma_{\mathrm{HEL}}. \tag{19}$$

For $\nu\approx 0.42$ (see below) and $\sigma_{\mathrm{HEL}}\approx 7.2$ GPa, $\sigma_Y\approx 2$ GPa, consistent with its values near the onset of plasticity; see the steady state values at $u_p=0.25$ and 0.375 km s^{-1} (Fig. 6), as well as the onset strength for $u_p=0.5$ km s^{-1} in Fig. 4(b). Although σ_Y at HEL can be estimated with reasonable accuracy from σ_{HEL} and ν, it may not be used for high pressures due to possible work hardening or softening.

Given $\sigma_{ij,H}$, the Poisson's ratio and hydrostaticity are calculated for different steady shock states (Table I). It is expected that increasing strain softening with increasing shock strength corresponds to increasing ν (to 0.5) and h (to 1), and this indeed agrees with our observations. The shocked metallic glass is not completely hydrostatic at $u_p<1$ km s^{-1}, and retains finite shear strength up to 1 km s^{-1}, likely due to unsaturated (but successively growing) plasticity. However, since the values of ν and h are high even at the onset of plasticity, the u_s-u_p relation in the plastic regime can essentially be described by a single linear relation with $c_0\approx c_B$ (Fig. 5).

The opposing rarefaction fans encounter within the target, releasing the shock compressed region into a tensile state; when this tensile stress exceeds a critical strength, spall is initiated after some short delay. This maximum tensile stress ($-\sigma_{11,\max}$) is the dynamic spall strength σ_{sp}. σ_{11} and T in the spall region then increase due to recompression, but the average density decreases due to void nucleation and growth, which is characteristic of the spall process (Fig. 7). Multilayer spallation is observed: $-\sigma_{11}$ can reach the spall strength at several locations throughout a broad spall zone (e.g., the profile at 89 ps in Fig. 2), and nucleate multiple spall layers (Fig. 1 and the 93-ps profile in Fig. 2). Compression waves are originated at the spall zone and propagate toward the free surfaces of the flyer plate and target, inducing a pullback in $u_{\mathrm{fs}}(t)$ (e.g., $u_p=0.5$ km s^{-1} in Fig. 3). The subsequent release and compression waves are then trapped between the spall zone and the target (or flyer plate) free surface, yielding reverberations in $u_{\mathrm{fs}}(t)$ (not shown).[21]

The instantaneous tensile strain rate can be obtained from the spatial derivatives of $u_1(x)$ and $\rho(x)$ with the Eulerian mass conservation equation

$$\dot{\varepsilon}=\left(\frac{\partial u_1}{\partial x}+\frac{u_1}{\rho}\frac{\partial \rho}{\partial x}\right)\Bigg|_t. \tag{20}$$

The second term on the right hand side of Eq. (20) can be omitted near the maximum tensile stress zone (where $\partial\rho/\partial x$ is small). $\dot{\varepsilon}$ may vary with x and t, and its value in the spall zone right before the spall initiation is adopted. While higher strain rate normally increases spall strength, the temperature in the spall zone right before spallation (or simply, spall temperature T_{sp}) has an opposite effect. Thus, the spall parameters include σ_{sp}, $\dot{\varepsilon}$ and T_{sp}. Spallation occurs at $u_p\geq 0.5$ km s^{-1} in our simulations, and the related spall parameters are summarized in Table I. With increasing u_p, both T_{sp} and $\dot{\varepsilon}$ increase, while σ_{sp} increases then decreases due to the competing effects of T_{sp} and $\dot{\varepsilon}$.[36]

B. Plasticity and spallation mechanisms

Amorphous metallic glasses lack well-defined crystal lattices and, consequently, prohibit plastic deformation via long-range concerted movement of atoms. Therefore, the observed plasticity cannot be explained with the conventional crystal plasticity theory (e.g., dislocations)[58] and we resort to the local shear strain analysis in terms of η^{vM}.[11]

For a configuration under consideration, η^{vM} is calculated relative to a fixed reference frame, the initial configuration prior to shock loading. Across the shock front, η^{vM} increases from its ambient value of about 0.04 in the unshocked region (due to thermal fluctuations) gradually to a steady shock state value [Figs. 4(c) and 8]. For $u_p=0.5$ km s^{-1}, the two-wave structure in $\sigma_{11}(x)$ and the profile of $2\tau=(\sigma_{11}-\sigma_{22})$ [Figs. 4(a) and 4(b)] clearly show the elastic-plastic transition which is accompanied by the accordant increase in η^{vM}. While the elastic-plastic transition thickness as seen from $\sigma_{11}(x)$ is about 2000 Å, it is nearly 50% wider in $2\tau(x)$ and $\eta^{\mathrm{vM}}(x)$, indicating the shear properties appear to have slower

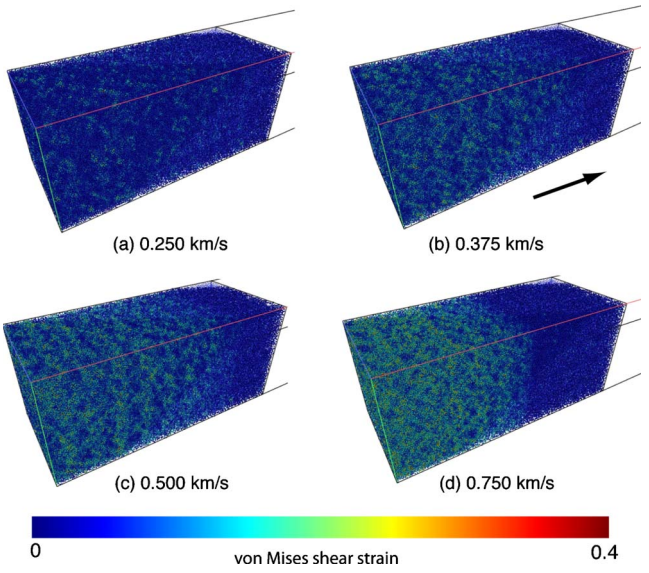

FIG. 8. (Color online) Visualization of the $Cu_{46}Zr_{54}$ glass shock-loaded at different u_p in terms of η^{vM}. The cross-section (on the yz pane) is 16.8 nm × 16.8 nm. The arrow denotes the shock direction x.

relaxation kinetics. The shock-state η^{vM} increases with increasing u_p (Fig. 8 and circles in Fig. 9): it is close to the ambient value below the HEL (e.g., at u_p=0.125 km s^{-1}), becomes noticeable above the HEL, and then saturates at high u_p. The elastic precursor is not pronounced in $\eta^{vM}(x)$,

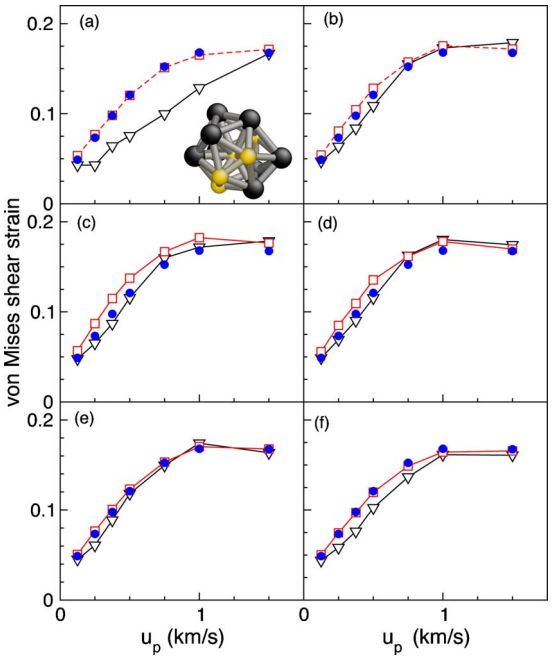

FIG. 9. (Color online) The averaged shock-state η^{vM} for the atoms conserving the original Voronoi type (or conserved; triangles), the transformed atoms (squares) and the bulk (circles). (a–f) refer to Voronoi Types 1–6, respectively. The inset to (a) is a Type 1 Voronoi polyhedron centered at a Cu atom with its 12 Cu and Zr nearest neighbors forming an icosahedron, indexed as $\langle 0,0,12,0\rangle$.

likely due to the low threshold of $\eta^{vM} \sim 0.06$ for the elastic-plastic transition as identified from Figs. 4(c) and 9; another reason is that $\eta^{vM}(x)$ is averaged over a finite bin width around a given x, and a few nuclei will be overwhelmed by the ambient surroundings as a result. The shear strain is inhomogeneous at nm scales: the localized high shear strain zones or simply shear transformation zones (STZs) are limited in size (sub-nm in width initially) and dispersed among low shear zones. No preferred growth of certain STZs are observed in our simulations, likely due to the simulation geometry (the y and z directions are constrained rather than free). The STZs are randomly centered, but are regularly shaped with two intersecting branches; each branch is at about ±45° from the shock direction in the xy and xz planes, i.e., along the maximum shear stress directions as expected. Such a STZ pattern was also observed in a $Cu_{64}Zr_{36}$ glass sheet under uniaxial tension, simulated with an embedded-atom-method potential.[14] Similarly, STZs occurred in MD simulations of ternary and quinternary glasses under pure shear and uniaxial stress loading.[11,13] STZs were examined in both nanoparticle and bulk NiZr glasses;[15,16] the STZ pattern similar to ours was found in this bulk glass with the atomic bond angle distribution peaked at 45°, while the bond angle distribution is broad for nanoparticles.[15] As noted by Schuh *et al.*,[4] STZs comprising a few to hundreds of atoms are commonly observed in computer simulations spanning a wide range of glass compositions, interatomic potentials and (nonshock) loading conditions. Thus, these previous MD simulations, together with our current work, strongly suggest that STZs are a common mechanism of plastic deformation in metallic glasses under both shock and nonshock loading conditions.

The elastic-plastic transition is sluggish for u_p =0.25–0.5 km s^{-1}, and the thickness of the plastic shock wave front decreases (i.e., steepens) at higher u_p. The transition is dominated by the relaxation process of $2\tau=(\sigma_{11}-\sigma_{22})$ from its overshoot peak over HEL likely due to transient strain hardening [e.g., at about 13000 Å, Fig. 4(b)]; this transient overshoot determines the relaxation kinetics and the plastic shock thickness. For example, the amount of overshoot increases from about 0.8 GPa for u_p=0.5 km s^{-1} to 3–4 GPa for 1 km s^{-1}, and reduces the plastic shock thickness from about 2000 Å to 200 Å accordingly. The strain hardening is also observed in some experiments,[63] and can be explained with the exhaustion of STZ nucleation sites;[3] this is indeed the case as we will show below in Sec. III C. For comparison, the observed shock-state strain softening (Fig. 6) is also related to local structure features (Sec. III C) besides the shock heating effect, as suggested by Schuh *et al.*[4] Higher shock strength increases STZs and induces higher temperature, which in turn facilitates the plastic transformation, but this factor is possibly secondary at the onset of plastic deformation. In contrast to the rapid plasticity kinetics and high plasticity at high u_p, the slow kinetics at low u_p induce low plasticity in the shocked region, which is nonetheless in a supported shock state in our MD time scales; this underdeveloped (unsaturated) plasticity gives rise to the relatively high shear strength and low hydrostaticity at low u_p (Table I and Fig. 6).

We also calculate the local atomic temperatures during shock loading and compare them with the corresponding η^{vM}

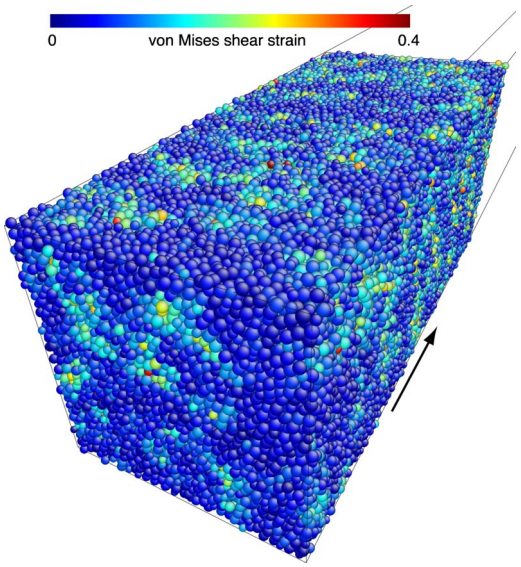

FIG. 10. (Color online) Visualization of a slice of the $Cu_{46}Zr_{54}$ glass at a fully released state (zero stress) after unloading from the shock state (u_p=0.5 km s^{-1}). The cross-section (on the yz pane) is 8.4 nm×8.4 nm. The arrow denotes the shock direction x. Color coding is based on η^{vM}.

and no good correlation between T and η^{vM} is found, i.e., the temperatures in the STZs are comparable to those in the low shear zones. Local temperature variations are not the cause for STZ (the local structures are instead, see Sec. III C), and not the effect of STZ, either. The latter is probably attributed to the slower kinetics in thermalization than strain relaxation upon shock loading with finite shock thicknesses. Thus, initiation of STZ is of structural rather than thermal origin. Similarly, MD simulations on different metallic glasses suggest that the thermal effect becomes important only after the STZ reaches a critical size.[11]

During release (unloading), the STZs can still persist, although the exact deformation may vary with time and impact velocity; Fig. 10 shows STZs at a completely released state. Shear bands were well observed in a Zr-based metallic glass recovered after shock loading.[24] Following unloading, the glass is subjected to tensile loading, and the configuration near the onset of spallation (prespall, cf. Figure 2) undergoes additional shear strain compared to their earlier shock state counterparts. For example, the average η^{vM} is about 0.12 at the shock state for u_p=0.5 km s^{-1}, and it increases to about 0.18 right before spall after release fan induced tensile loading beyond compression. The prespall η^{vM} is about 0.2 if referenced to the shock state. STZs also grow in size (Fig. 7 vs Fig. 8) over the course of shock compression, release and tension, and can be better correlated with local temperature before spall (compared to the correlation at the shock state), likely because of the longer time scales allowing heating from shear strain (plastic heating). We have shown that void nucleation in shock-loaded single crystal Cu is preceded by crystal plasticity and other defect formation, and occurs preferentially at the regions with high disordering and plasticity.[64] (Similar behavior is observed for Ni under shock and Lennard-Jones face-centered cubic crystals and single crystal Cu under nonshock conditions.)[33,35,65] Preferential nucleation of voids in disordered regions was observed in a shock-loaded crystalline glass-forming crystalline (B11) CuTi alloy.[41] Void nucleation is found to favor shear bands in shock-recovered crystalline alloys[20] and bulk metallic glass.[24] As expected, the snapshots in Fig. 7 show that void nucleation occurs at highly shear-deformed regions (high plasticity) in the amorphous metallic glass. Thus, the predamage in terms of plasticity as well as certain defect formation is prerequisite and likely common for void nucleation in both crystalline and amorphous metals.

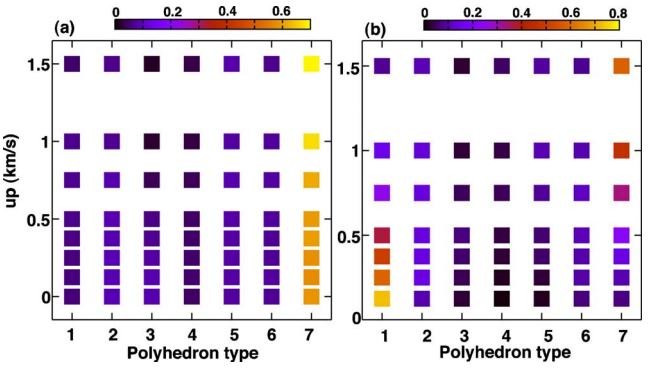

FIG. 11. (Color online) (a) The atomic fraction vs Voronoi polyhedron type at different shock states and ambient conditions. Each atom belongs to a certain Voronoi type (Types 1–7) based on the Voronoi analysis. (b) The fractions of the original Type 1 atoms transforming into other types at different shock states (transformed). The fraction of Type 1 atoms in the unshocked state is 1. The conserved fraction is also included (atoms remaining as Type 1 after shock loading).

C. Structural features related to plasticity and spall

The microscopic structures of the unshocked and shocked $Cu_{46}Zr_{54}$ glasses are characterized with the Voronoi analysis method, in which each atom is indexed with four Voronoi indices and assigned a Voronoi polyhedron type. As described in Sec. II, Types 1–6 are individual Voronoi types, and Type 7 is a collective Voronoi type consisting of numerous other minor individual types such as ⟨0,2,8,3⟩, ⟨0,4,4,3⟩, ⟨1,0,9,3⟩, and ⟨0,12,2,0⟩. Shown as an example in Fig. 9(a) inset is a Type 1 Cu atom (indexed as ⟨0,0,12,0⟩) with its 12 Cu and Zr nearest neighbors forming an icosahedron around it. The fractions or percentages of Voronoi Types 1–7 are calculated referencing to the total number of atoms in a region under consideration, and shown in Fig. 11(a) for the ambient and shock states at different u_p.

In the unshocked glass (u_p=0), the atoms indexed as Types 1–6 are predominant in quantity over all other individual types included in Type 7. The fraction of Type 1 atoms (icosahedron) is about 0.05; among all the Type 1 polyhedra, the majority is Cu centered and the Zr-centered polyhedra account for ~9%, consistent with previous studies.[54,66,67] The fraction of Type 3 atoms is about 0.09, and most Type 3 polyhedra are also Cu-centered. ⟨0,12,2,0⟩ is an example of Type 7; all polyhedra indexed as ⟨0,12,2,0⟩ are Zr-centered and likely related to the Frank-

Kasper polytetrahedra.[68] As a collective type, however, the fraction of Type 7 atoms (>0.5) prevails over Types 1–6 in unshocked and shocked states. Types 1–6 represent relatively "close-packed" atoms, and are expected to diminish with increasing shock strengths overall. With increasing u_p, the fractions of Types 2–4 decrease, that of Type 1 increases slightly and then decreases rapidly, and those of Types 5 and 6 remain nearly constant, while that of Type 7 increases from about 0.6 at $u_p=0$ to 0.7 at 1.5 km s^{-1}. The decrease in Type 3 contributes to about 70% of the increase in Type 7 over the whole u_p range explored. Above HEL, the atoms of Type 3 decrease rapidly within $u_p=0.25-1.0$ km s^{-1} and, Types 2 and 4, within 0.5–1.0 km s^{-1}, consistent with the pronounced softening above 0.375 km s^{-1} (Fig. 6).

Upon shock loading, the Voronoi type of an atom can change, e.g., the original Type 1 may transform *into* another type (Types 2–7) after shock, and a Type 1 atom at the shock state may have transformed *from* another type. For illustrative purpose, we characterize such transformations between Type 1 and other types at different steady shock states. Figure 11(b) shows the case of transformation from Type 1 into Types 1–7. With increasing u_p, the conserved fraction (Types $1\rightarrow1$, or simply $1\rightarrow1$) decreases rapidly from about 0.73 at $u_p=0.125$ km s^{-1} to 0.08 at 1.5 km s^{-1}; the conserved Type 1 atoms are highly shear resistant (see below) and their decrease is consistent with the strain softening (Fig. 6). The fractions of the original Type 1 atoms transforming into Types 3 and 4 are largely negligible. The $1\rightarrow7$ transformation is the most pronounced overall in particular at the high u_p end, followed by the $1\rightarrow2$, $1\rightarrow6$ and $1\rightarrow5$ transformations in descending order. The $1\rightarrow2$ transformation is favored at the low u_p end, and $1\rightarrow5$, the high u_p end. For the transformations into Type 1 at the shock states (not shown), the general feature is mainly similar to their inverse transformations [Fig. 11(a)] except for a more pronounced $3\rightarrow1$ transformation (compared to its inverse) above HEL. The frequent occurrence of the $1\leftrightarrow2$ transformations (only less frequent than $1\leftrightarrow7$) may be explained by their structural similarity. As a result of the forward and backward transformations, the fraction of Type 1 atoms undergoes a minor increase and then faster decrease with increasing u_p. As noted previously,[54] such transformations as $1\rightarrow5$ induce excess volumes, which may lend some support to the free volume model of plasticity in metallic glasses.[3–5]

Given the Voronoi analysis at different shock states, we characterize the shear mobility (m) of a Voronoi atom type in terms of η^{vM} at different shock strengths (Fig. 9). For each original (before shock) Voronoi type (Types 1–6), we divide the corresponding atoms within a selected steady shock region into two groups, the conserved and transformed atoms; the average shear strain is calculated for each group, and compared to the bulk average of all the atoms under consideration, which serves as the baseline for comparison. Overall, the conserved atoms undergo smaller shear strain than the transformed atoms, and the difference is diminished at the high u_p end. For the transformed atoms, $m_1\approx m_6\approx m_5<m_2<m_4<m_3$ (subscripts denote the Voronoi types); for the conserved atoms, $m_1<m_6<m_2<m_5\approx m_4\approx m_3$. The difference in the shear mobility between conserved and transformed atoms is the largest for Type 1 and smallest for Type 5; and the average mobility for a given type (including both conserved and transformed) is the highest for Type 3 and smallest for Type 1. Thus, Type 3 atoms are most mobile (Type 4 is similar but less important due to its low concentration); Type 1 atoms are most shear-resistant, similar to previous observations.[54,67] Type 5 atoms are most likely to follow the bulk behaviors. Type 6 is similar to Type 1 in the general trend. The high shear mobility of Type 3 atoms also dictates their low structural stability under shear stress; as shown in Fig. 11(a), the fraction of Type 3 decreases continuously to nearly zero with increasing u_p. The major increase in the shear strain occurs at $u_p=0.5-1.0$ km s^{-1} for Types 1–6 (Fig. 9), which partly reduces the fractions of such types as Type 3 [Fig. 11(a)]. Note that the shear strain of the conserved Type 1 atoms is constant below and near HEL and then increases rapidly above HEL; thus, one manifestation of the plasticity is the sharp increase in the shear mobility of conserved Type 1 atoms.

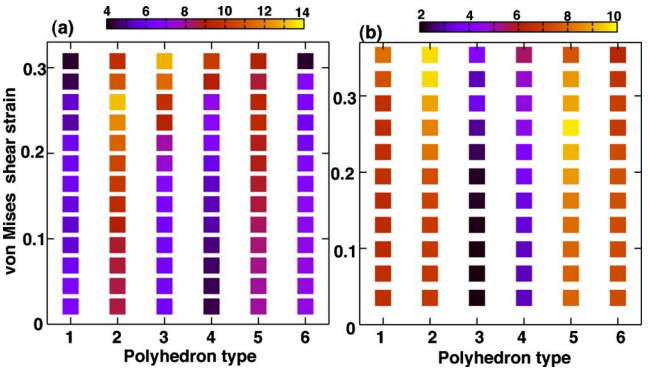

FIG. 12. (Color online) The percentage of a specific Voronoi type vs. shear strain at the shock states with (a) $u_p=0.5$ km s^{-1} and (b) 1 km s^{-1}. Color coding is based on the cumulative percentage above a certain η^{vM}.

We also examine the distributions of Types 1–7 in the whole range of η^{vM} within a steady shock region. This η^{vM} range is divided into 20 bins, each centered at certain η^{vM}; and the number of atoms of each type within each bin is counted. The cumulative number of atoms above a certain η^{vM} is obtained as well. The corresponding percentages are calculated, and Fig. 12 shows the examples of such distributions at two representative shock states, $u_p=0.5$ and 1.0 km s^{-1} (only the cumulative distributions are shown). At $u_p=0.5$ km s^{-1} [Fig. 12(a)], the percentages of Types 1 and 6 decrease with increasing η^{vM} (favoring low η^{vM} as observed previously),[14] in sharp contrast to Types 2–5 (favoring high η^{vM}); these observations are consistent with their shear mobilities (or resistances). In particular, Type 1 is most abundant at the lowest shear strains, and Type 3, the highest strains (excluding Type 7). Thus, the high shear mobility of Type 3 (as well as Types 2, 4, and 5 to a lesser extent) atoms play the dominant role in the formation of STZs, and Type 1 (as well as Type 6) atoms, in forming lower strain regions distinct from STZs. The distribution of Type 7 is approximately uniform (minor decrease in the fraction with increasing η^{vM}). All these types act collectively to induce the inhomogeneous shear deformation at the atomic level that leads to plastic flow. At $u_p=1.0$ km s^{-1} [Fig. 12(b)], the general

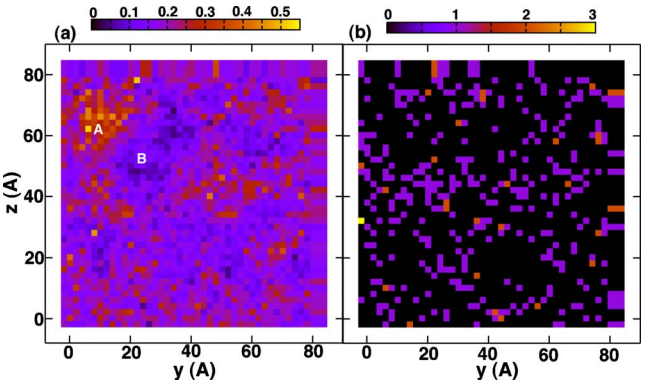

FIG. 13. (Color online) The prespall η^{vM} distribution (a) and the corresponding distribution of Type 1 and 6 atoms in a thin section for u_p=0.5 km s^{-1} at 87.2 ps, viewed along the shock direction. In (a), *A* denotes a high η^{vM} region (void nucleation site), and *B*, a low η^{vM} region. In (b), color coding refers to the number of Type 1 or 6 atoms in a fine grid on the *yz* plane.

trend remains similar with some exceptions. Types 1 and 6 are enriched relative to Types 2–5, and Types 2 and 5 become most abundant at highest η^{vM}. The drastic changes lie in Type 3, which is almost absent at the low η^{vM} end and reduced greatly at the high end, simply because of its low stability at high shock strengths due to its high shear mobility. The total fraction of Type 3 is reduced [Fig. 11(a)] again due to its low structural stability.

Similar to the plasticity nucleation and shock state strain softening as discussed above, the transient hardening [Fig. 4(b)] can also be attributed to the atomic-level structural evolution. At the onset of plasticity (just above HEL), we find that the fraction of Type 3 atoms decreases while 2τ increases transiently, and thus the nucleation sites are reduced since Type 3 atoms play a predominant role in STZ nucleation. As argued by Chen,[3] the critical shear stress driving the formation of STZ will increase in order to sustain a plastic deformation rate as the nucleation sites exhaust, thus giving rise to the transient strain hardening. Indeed, we observe that such hardening increases with increasing loading rate (or u_p).

During release and tension induced by the reflected shock waves, the solid undergoes further shear deformation and structure changes, and nanovoids nucleate in the regions with high shear deformations [Figs. 7 and 13(a)]. As an illustrative case relating void nucleation to local structures for low and medium u_p (the shock regime of main interest), we cut a thin slice out of the prespall atomic configuration perpendicular to the shock direction through the void nucleation region for u_p=0.5 km s^{-1}; the Voronoi type and η^{vM} for each atom within this slice are calculated prior to slicing. The highest η^{vM} ($>$0.3) region is dominated by the atoms of Type 2–5 (in particular Type 3; excluding Type 7), where Type 1 and 6 atoms are minimum [similar to Fig. 12(a)]. In the spatial distributions of η^{vM} and the Voronoi types, region *A* is occupied by atoms with the highest shear deformation [Fig. 13(a)] while few Type 1 or 6 atoms are present [Fig. 13(b)]. On the other hand, Types 1 and 6 are much more abundant in the least shear-deformed regions (e.g., η^{vM} $<$0.05, region *B*). Thus, the regions with prone-to-shear-flow Type 3 atoms are also favored for void nucleation, in sharp contrast to Type 1 atoms with highest shear resistance. However, we do not expect an exact one-to-one spatial correspondence between a local structure and the shear deformation in the whole region. Note that these structural features related to void nucleation are only approximate since the glass is more homogenized after release and tension compared to the shock state. At high shock strengths, fewer Type 3 atoms are found for the same reason of high shear mobility as in the shock state; void nucleation still occurs at the highly shear-deformed regions during tension, but the exact structural features vary because of different shock state structures and subsequent relaxation during release and tension.

The complex structural changes among different Voronoi polyhedron types are observed in our simulations, and the formation and evolution of STZs are accompanied by these changes in a dynamic way. Possible mechanisms underlying such changes include the free volume theory and the bond-exchange model;[69,70] the latter was proposed by Egami and co-workers to describe the shear deformation in glasses. On one hand, the free volume theory is appealing since free volume is necessary for local shear transformation,[69] and such transformations as Types $1 \rightarrow 5$ induce excess volumes.[54] On the other hand, the atomic bond rearrangement is more realistic as suggested by Egami.[69] Egami argued that deformation should involve changes in bond arrangement if the structure is defined by the topology of atomic connectivity, and proceeds via bond exchange when the total number of bonds is conserved during rearrangement. A recent MD simulations on a binary metallic glass show that transitions between distinct polyhedron types may occur at ps time scale and give rise to the boson peak.[71] The structure changes in our simulations could be candidates for such topological structure changes, and thus the bond rearrangement appears to be a highly plausible mechanism. Guerdane and Teichler[71] also pointed out that in icosahedral-like medium range orders, the coupling between neighboring structural units leads to dependencies between their local environment transitions and induces an atom exchange between them, in a way similar to the bond-exchange model; this argument lends further support to the bond-rearrangement mechanism.

IV. CONCLUSIONS

We have characterized the shock states, plasticity, shear flow strength, spallation, and related structural features of $Cu_{46}Zr_{54}$ metallic glasses under adiabatic 1D strain shock wave loading. The plasticity is manifested as STZs. Our work and previous results by others suggest that STZ appears to be common to the plastic deformation in metallic glasses under both shock and nonshock loading conditions. Transient strain hardening and shock-state softening are observed, and can be related to the evolution dynamics of STZs. The void nucleation for spallation occurs preferentially at highly shear-deformed sites. The Voronoi and local shear strain analyses show that atoms with different local environments, characterized in terms of Voronoi polyhedron types, have

different shear resistances. In particular, the atoms indexed with $\langle 0,0,12,0\rangle$ are most shear-resistant, and those with $\langle 0,2,8,1\rangle$ are highly prone to shear flow. This atomic-level structural inhomogoneity leads to inhomogeneous shear deformation and thus STZs, which in turn play a key role in plasticity as well as void nucleation and growth. STZ is of structural rather than thermal origin (at least at current MD time scales). The local atomic structures may change dynamically in response to loading and unloading. Such complex structure changes could be achieved via the bond exchange or rearrangement as suggested for topological structure changes.

ACKNOWLEDGMENTS

We have benefited from discussion with S. Valone. This work has been supported by the Laboratory Directed Research Development programs at LANL. LANL is operated by Los Alamos National Security, LLC for the U.S. Department of Energy under Contract No. DE-AC52-06NA25396.

*sluo@lanl.gov
†Tahir.Cagin@chemail.tamu.edu

[1] W. L. Johnson, J. Miner. Met. Mater. Soc. **54**, 40 (2002).
[2] A. L. Greer and E. Ma, MRS Bull. **32**, 611 (2007).
[3] M. W. Chen, Annu. Rev. Mater. Res. **38**, 445 (2008).
[4] C. A. Schuh, T. C. Hufnagel, and U. Ramamurty, Acta Mater. **55**, 4067 (2007).
[5] W. H. Wang, C. Dong, and C. H. Shek, Mater. Sci. Eng. R. **44**, 45 (2004).
[6] F. Varnik, L. Bocquet, J. L. Barrat, and L. Berthier, Phys. Rev. Lett. **90**, 095702 (2003).
[7] B. Yang, M. L. Morrison, P. K. Liaw, R. A. Buchanan, G. Y. Wang, C. T. Liu, and M. Denda, Appl. Phys. Lett. **86**, 141904 (2005).
[8] H. Bei, Z. P. Lu, and E. P. George, Phys. Rev. Lett. **93**, 125504 (2004).
[9] Y. F. Shi and M. L. Falk, Phys. Rev. Lett. **95**, 095502 (2005).
[10] C. A. Schuh and A. C. Lund, Nature Mater. **2**, 449 (2003).
[11] F. Shimizu, S. Ogata, and J. Li, Mater. Trans. **48**, 2923 (2007).
[12] S. Ogata, F. Shimizu, J. Li, M. Wakeda, and Y. Shibutani, Intermetallics **14**, 1033 (2006).
[13] Y. Q. Cheng, A. J. Cao, H. W. Sheng, and E. Ma, Acta Mater. **56**, 5263 (2008).
[14] A. J. Cao, Y. Q. Cheng, and E. Ma, Acta Mater. **57**, 5146 (2009).
[15] F. Delogu, Phys. Rev. B **77**, 174104 (2008).
[16] F. Delogu, Phys. Rev. B **79**, 184109 (2009).
[17] S. G. Mayr, Phys. Rev. B **71**, 144109 (2005).
[18] G. E. Duvall and R. A. Graham, Rev. Mod. Phys. **49**, 523 (1977).
[19] R. G. McQueen, S. P. Marsh, J. W. Taylor, J. N. Fritz, and W. J. Carter, in *High Velocity Impact Phenomena*, edited by R. Kinslow (Academic, New York, 1971), p. 314.
[20] M. A. Meyers, *Dynamic Behavior of Materials* (Wiley, New York, 1994).
[21] T. Antoun, L. Seaman, D. R. Curran, G. I. Kanel, S. V. Razorenov, and A. V. Utkin, *Spall Fracture* (Springer, New York, 2003).
[22] Ya. B. Zel'dovich and Yu. P. Raizer, *Physics of Shock Waves and High-Temperature Hydrodynamic Phenomena* (Dover, Mineola, 2002).
[23] D. E. Grady, J. Mech. Phys. Solids **36**, 353 (1988).
[24] S. Zhuang, J. Lu, and G. Ravichandran, Appl. Phys. Lett. **80**, 4522 (2002).
[25] M. Martin, T. Sekine, T. Kobayashi, L. Kecskes, and N. N. Thadhani, Metall. Mater. Trans. A **38A**, 2689 (2007).
[26] H. Togo, Y. Zhang, Y. Kawamura, and T. Mashimo, Mater. Sci. Eng., A **449-451**, 264 (2007).
[27] F. Yuan, V. Prakash, and J. J. Lewandowski, J. Mater. Res. **22**, 402 (2007).
[28] S. J. Turneaure, J. M. Winey, and Y. M. Gupta, Appl. Phys. Lett. **84**, 1692 (2004).
[29] B. L. Holian, Shock Waves **5**, 149 (1995).
[30] B. L. Holian and P. S. Lomdahl, Science **280**, 2085 (1998).
[31] E. Dekel, S. Eliezer, Z. Henis, E. Moshe, A. Ludmirsky, and I. B. Goldberg, J. Appl. Phys. **84**, 4851 (1998).
[32] D. L. Paisley, S. N. Luo, S. R. Greenfield, and A. C. Koskelo, Rev. Sci. Instrum. **79**, 023902 (2008).
[33] J. Belak, J. Comput.-Aided Mater. Des. **5**, 193 (1998).
[34] M. A. Meyers, S. Traiviratana, V. A. Lubarda, D. J. Benson, and E. M. Bringa, JOM **61**, 35 (2009).
[35] S. G. Srinivasan, M. I. Baskes, and G. J. Wagner, J. Appl. Phys. **101**, 043504 (2007).
[36] S. N. Luo, Q. An, T. C. Germann, and L. B. Han, J. Appl. Phys. **106**, 013502 (2009).
[37] Q. An, S. N. Luo, L.-B. Han, L. Q. Zheng, and O. Tschauner, J. Phys.: Condens. Matter **20**, 095220 (2008).
[38] T. C. Germann, B. L. Holian, P. S. Lomdahl, and R. Ravelo, Phys. Rev. Lett. **84**, 5351 (2000).
[39] A. Strachan, T. Çağın, and W. A. Goddard III, Phys. Rev. B **63**, 060103(R) (2001).
[40] V. Dremov, A. Petrovtsev, P. Sapozhnikov, M. Smirnova, D. L. Preston, and M. A. Zocher, Phys. Rev. B **74**, 144110 (2006).
[41] Y. Ashkenazy and R. S. Averback, Appl. Phys. Lett. **86**, 051907 (2005).
[42] E. M. Bringa, J. U. Cazamias, P. Erhart, J. Stolken, N. Tanushev, B. D. Wirth, R. E. Rudd, and M. J. Caturla, J. Appl. Phys. **96**, 3793 (2004).
[43] A. Kubota, M.-J. Caturla, J. S. Stölken, and M. D. Feit, Opt. Express **8**, 611 (2001).
[44] S. N. Luo, L.-B. Han, Y. Xie, Q. An, L. Q. Zheng, and K. Xia, J. Appl. Phys. **103**, 093530 (2008).
[45] G. Duan, D. Xu, Q. Zhang, G. Zhang, T. Çağın, W. L. Johnson, and W. A. Goddard, Phys. Rev. B **71**, 224208 (2005).
[46] G. Duan, M. L. Lind, M. D. Demetrious, W. L. Johnson, W. A. Goddard, T. Çağın, and K. Samwer, Appl. Phys. Lett. **89**, 151901 (2006).
[47] J. L. Finney, Proc. R. Soc. London, Ser. A **319**, 479 (1970).
[48] J. L. Finney, Nature (London) **266**, 309 (1977).
[49] M. W. Finnis and J. E. Sinclair, Philos. Mag. A **50**, 45 (1984).
[50] M. I. Mendelev, D. J. Sordelet, and M. J. Kramer, J. Appl. Phys.

102, 043501 (2007).
[51] M. I. Mendelev, D. K. Rehbein, R. T. Ott, M. J. Kramer, and D. J. Sordelet, J. Appl. Phys. **102**, 093518 (2007).
[52] http://lammps.sandia.gov
[53] J. D. Honeycutt and H. C. Andersen, J. Phys. Chem. **91**, 4950 (1987).
[54] K.-W. Park, M. Wakeda, Y. Shibutani, E. Fleury, and J.-C. Lee, Met. Mater. Int. **14**, 159 (2008).
[55] Y. Q. Cheng, E. Ma, and H. W. Sheng, Phys. Rev. Lett. **102**, 245501 (2009).
[56] R. Hill, *The Mathematical Theory of Plasticity* (Clarendon, Oxford, 1950).
[57] L. M. Barker and R. E. Hollenbach, J. Appl. Phys. **43**, 4669 (1972).
[58] J. Lubliner, *Plasticity Theory* (Dover, New York, 2008).
[59] G. I. Kanel, S. V. Razorenov, and V. E. Fortov, *Shock-Wave Phenomena and the Properties of Condensed Matter* (Springer, New York, 2004).
[60] G. I. Kanel, S. V. Razorenov, A. S. Savinykh, A. Rajendran, and Z. Chen, J. Appl. Phys. **98**, 113523 (2005).
[61] B. G. Yoo and J. Jang, Mater. Res. Soc. Symp. Proc. **1049**, AA0501 (2008).
[62] J. Li, Modell. Simul. Mater. Sci. Eng. **11**, 173 (2003).
[63] J. Das, M. B. Tang, K. B. Kim, R. Theissmann, F. Baier, W. H. Wang, and J. Eckert, Phys. Rev. Lett. **94**, 205501 (2005).
[64] S. N. Luo, T. C. Germann, and D. L. Tonks, J. Appl. Phys. **106**, 123518 (2009).
[65] S. N. Luo, L. Q. Zheng, Q. An, and S. J. Zhao, Int. J. Mod. Phys. C **17**, 1551 (2006).
[66] X. D. Wang, Q. K. Jiang, Q. P. Cao, J. Bednarcik, H. Franz, and J. Z. Jiang, J. Appl. Phys. **104**, 093519 (2008).
[67] Y. Q. Cheng, E. Ma, and H. W. Sheng, Appl. Phys. Lett. **93**, 111913 (2008).
[68] N. Jakse and A. Pasturel, Phys. Rev. B **78**, 214204 (2008).
[69] T. Egami, Intermetallics **14**, 882 (2006).
[70] Y. Suzuki, J. Haimovich, and T. Egami, Phys. Rev. B **35**, 2162 (1987).
[71] M. Guerdane and H. Teichler, Phys. Rev. Lett. **101**, 065506 (2008).